

# Supplementary Information for

## Mitigating Polysulfide Crossover in Lithium–Sulfur Batteries with Polymer-Coated Separators

R. Blake Nuwayhid,<sup>1</sup> Junghoon Yeom,<sup>2</sup> Hunter O. Ford,<sup>1</sup> Zachary G. Neale,<sup>3</sup> Michael W. Swift,<sup>4</sup> Noam Bernstein,<sup>4</sup> Rachel E. Carter,<sup>3</sup> and Jeffrey W. Long<sup>3\*</sup>

<sup>1</sup>*National Research Council Postdoctoral Associate at the U.S. Naval Research Laboratory, Washington, DC, USA*

<sup>2</sup>*Multifunctional Materials Branch (Code 6350), U.S. Naval Research Laboratory, Washington, DC, USA*

<sup>3</sup>*Surface Chemistry Branch (Code 6170), U.S. Naval Research Laboratory, Washington, DC, USA*

<sup>4</sup>*Center for Materials Physics and Technology (Code 6390), U.S. Naval Research Laboratory, Washington, DC, USA*

\*Corresponding author: jeffrey.w.long26.civ@us.navy.mil

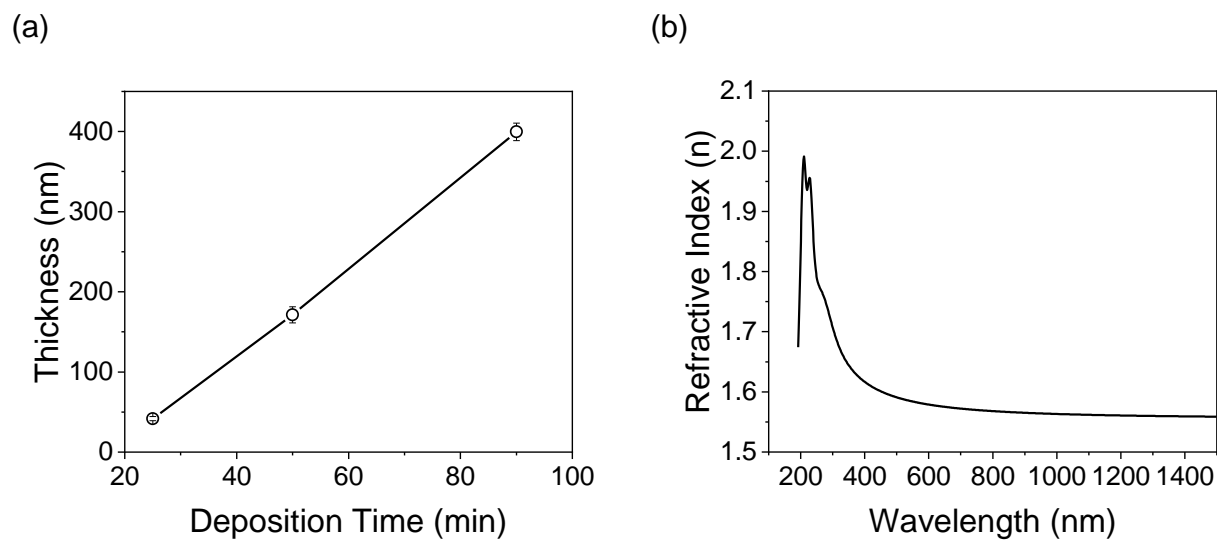


**Figure S1.** (a) Thickness values for 25-, 50-, and 90-minute depositions of pDVB-co-DMAMS, as determined by spectroscopic ellipsometry. Each point represents the average of measurements from two Si chips placed on opposite sides of the PE separators in the iCVD reactor in two separate depositions. (b) Refractive index as a function of wavelength for pDVB-co-DMAMS.

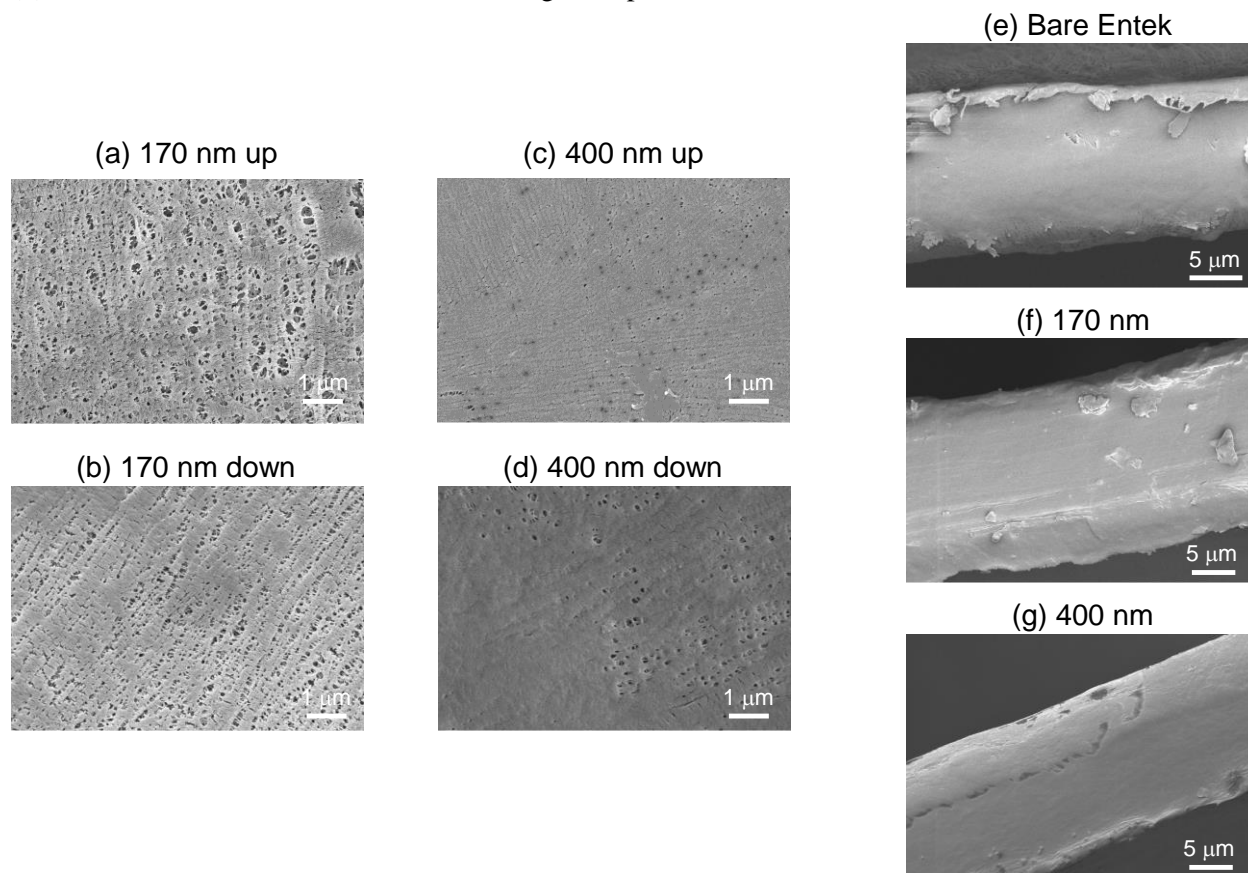


**Figure S2.** Scanning electron micrographs of top and bottom side of (a,b) 170nm-iCVD@PE and (c,d) 400nm-iCVD@PE separators in relation to their orientation in the iCVD reactor. Cross-sectional SEM images of (e) bare, (f) 170nm-iCVD@PE, and (g) 400nm-iCVD@PE separators.

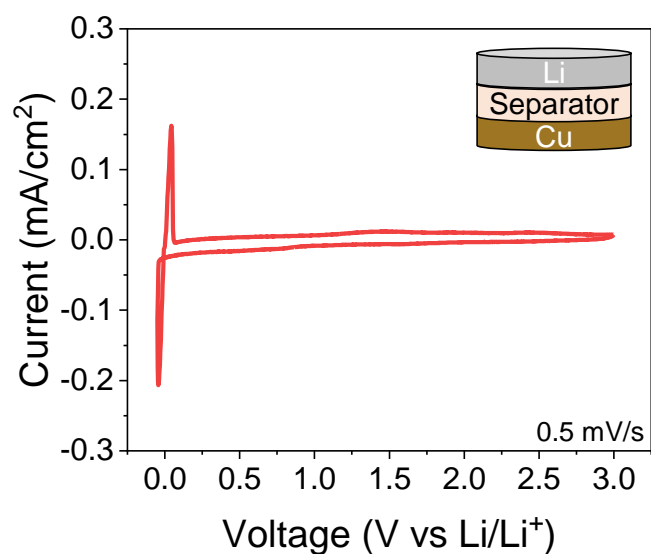


**Figure S3.** Cyclic voltammogram of a Li/Cu cell with a 170nm-iCVD@PE separator; cell scanned from  $-0.05$  V to  $3.0$  V at  $0.5$  mV/s, and with  $1$  M LiTFSI +  $0.2$  M LiNO<sub>3</sub> in DOL:DME electrolyte.

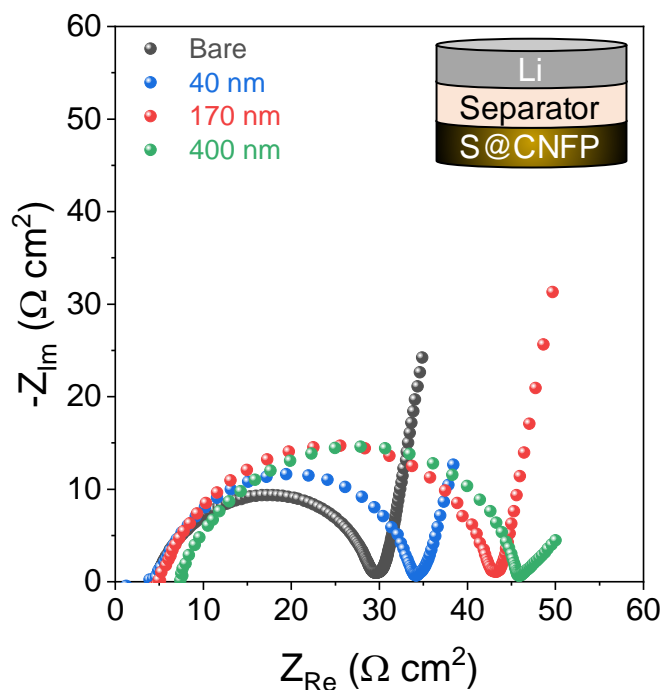


**Figure S4.** Nyquist plots from electrochemical impedance measurements of Li-S cells with bare, 40nm-, 170nm-, and 400nm-iCVD@PE separators, recorded after resting for 10 h following initial assembly and prior to charge-discharge cycling.

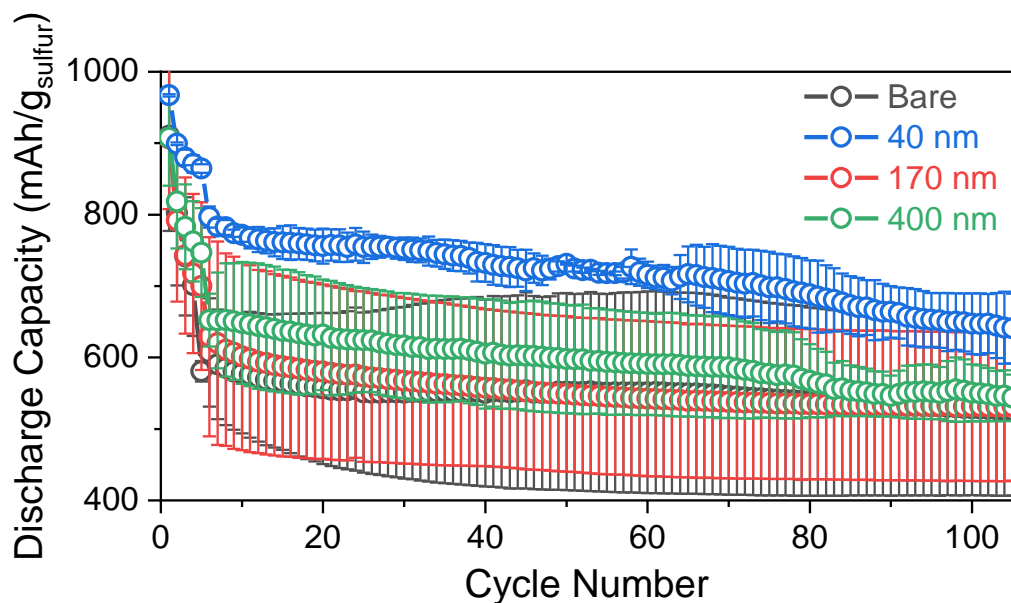


**Figure S5.** Average discharge capacity vs. cycle number (with error bars from two cells each) included for Li-S cells cycled with bare, 40nm-, 170nm-, and 400nm-iCVD@PE separators. The cycling rate is 0.1 A/g<sub>sulfur</sub> for the first 5 cycles (break-in) and 0.2 A/g<sub>sulfur</sub> for the following 100 cycles.

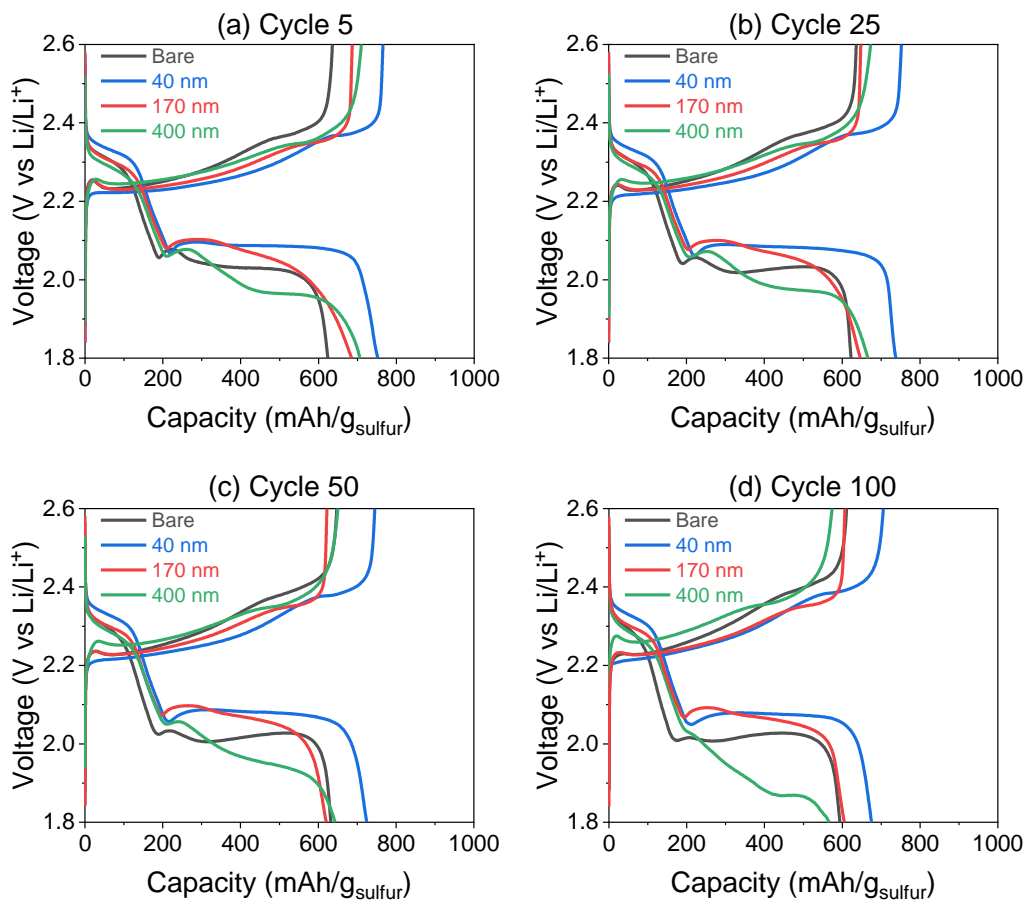


**Figure S6.** Charge-discharge voltage profiles from Li-S cells with bare separator, and 40nm-, 170nm-, and 400nm-iCVD@PE separators at the (a) 5<sup>th</sup>, (b) 25<sup>th</sup>, (c) 50<sup>th</sup>, and (d) 100<sup>th</sup> cycle. Cells were cycled at a normalized current of 0.2A/g<sub>sulfur</sub>.

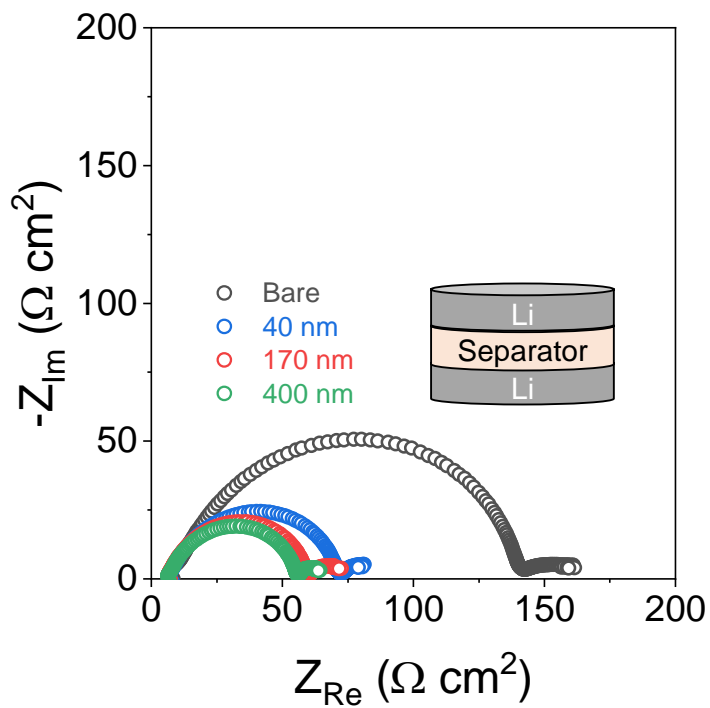


**Figure S7.** Nyquist plots from EIS measurements of Li/Li symmetric cells containing bare and iCVD@PE separators, recorded after resting for 24 h following assembly.

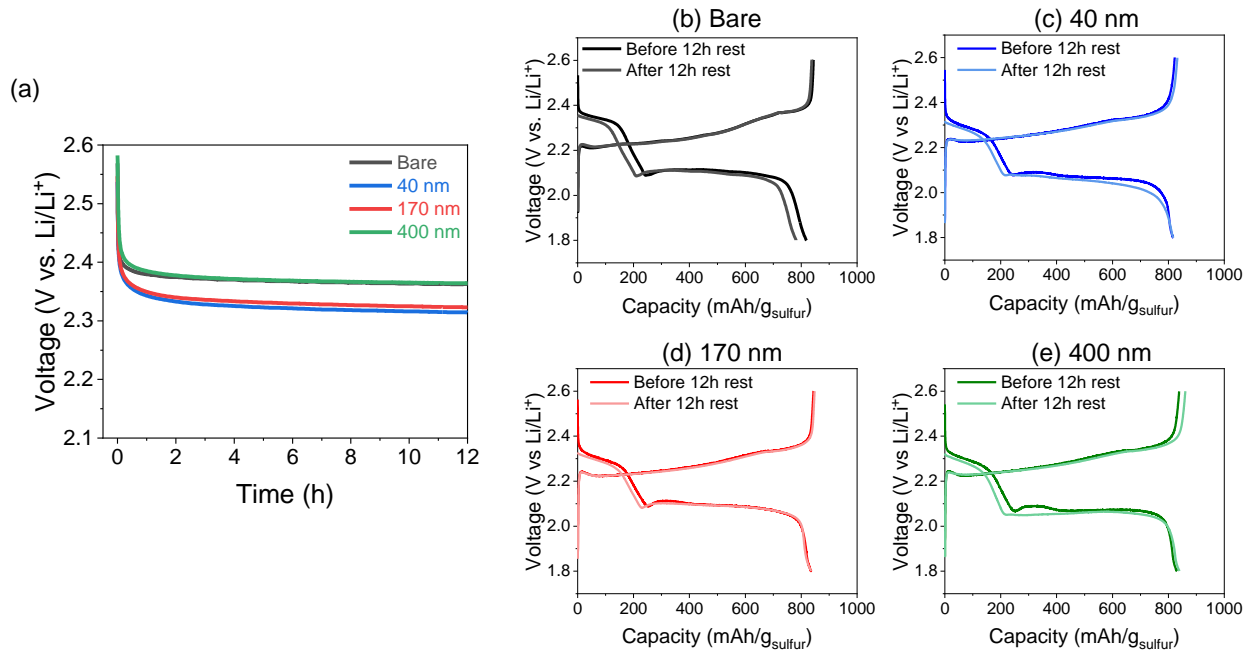


**Figure S8.** (a) Open-circuit voltage recorded for Li-S cells during a 12-h rest period after 10 charge-discharge cycles. (b-e) Charge-discharge voltage profiles of Li-S cells for cycle 10 before the 12-h rest period and for cycle 11 thereafter.

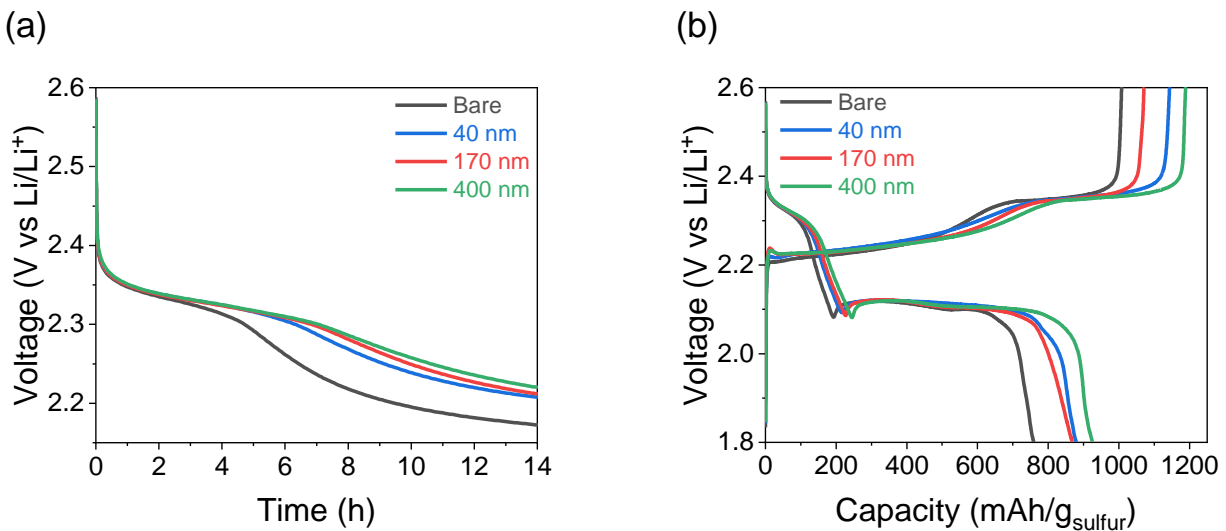


**Figure S9.** (a) Open-circuit voltage of Li-S cells without the LiNO<sub>3</sub> electrolyte additive during a 14-h rest period after 3 charge-discharge cycles. (b) Charge-discharge voltage profile for these cells before the extended rest period.

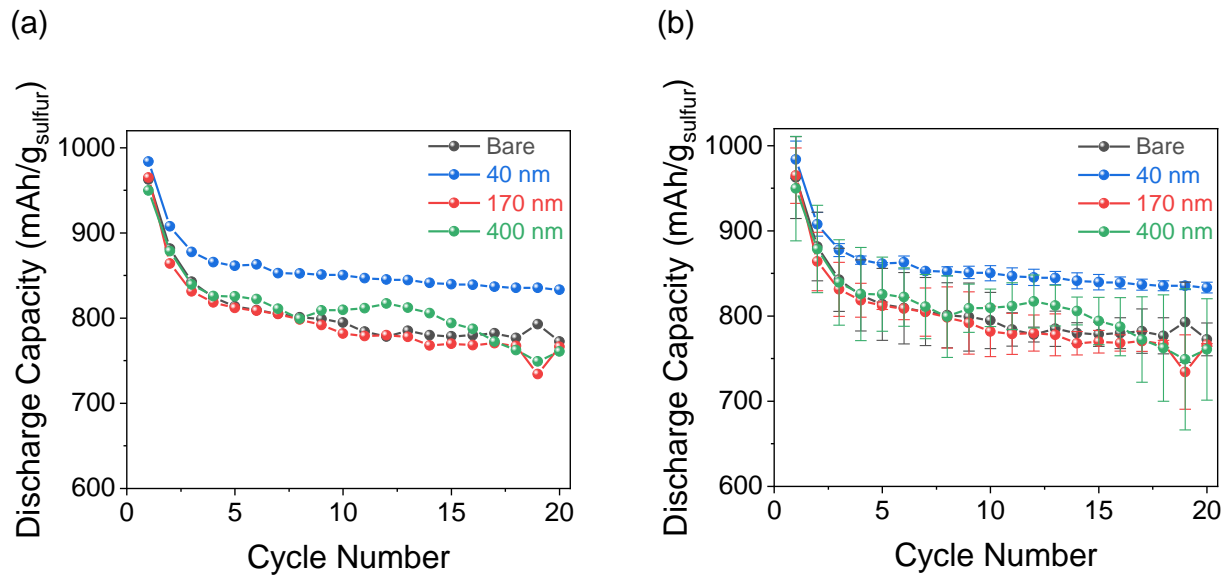


**Figure S10.** (a) Capacity-retention plots for the same Li-S cells subsequently analyzed with XPS and SEM, as shown in Figures 7-8. (b) Average discharge capacity and standard deviation for two cells with each pHVB-co-DMAMS separator-coating thickness. Cells cycled at 0.1 A/g<sub>sulfur</sub>.

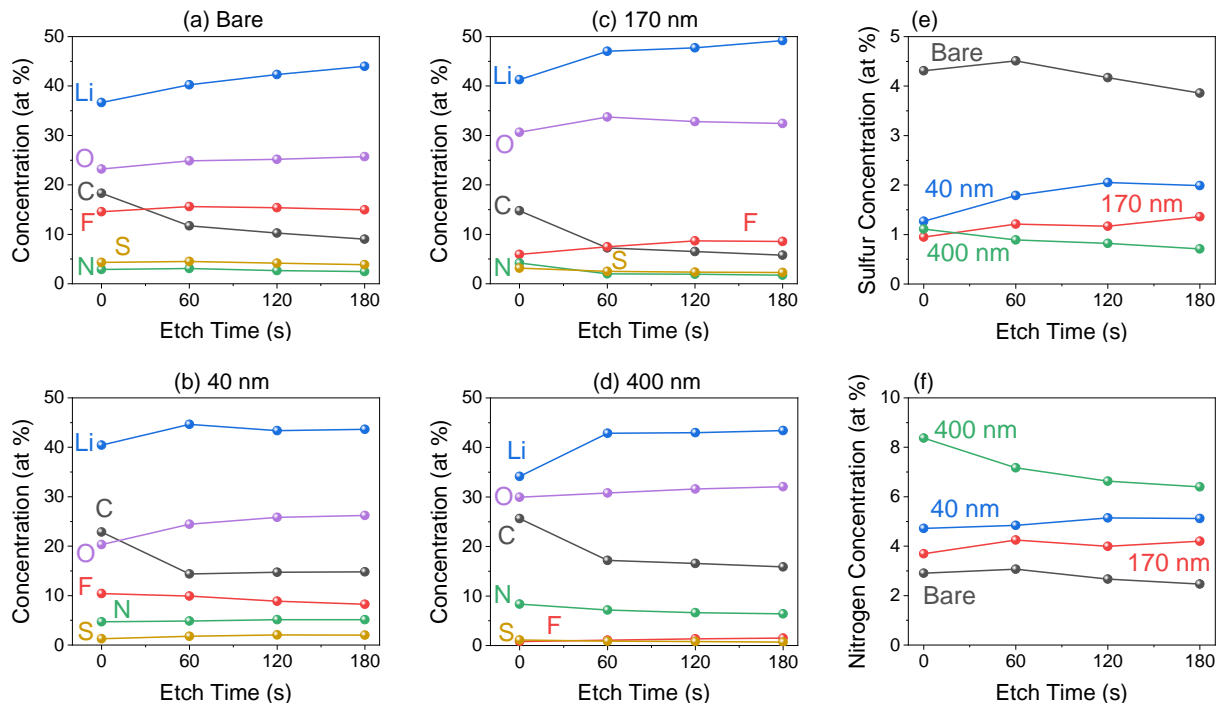


**Figure S11.** XPS depth-profile analysis of Li metal anodes after 20 cycles. (a-d) Atomic concentration profiles at the Li metal surface from cells cycled with bare, 40nm-, 170nm-, and 400nm-iCVD@PE separators. (e) Sulfur concentration profile and (f) nitrogen concentration profile.

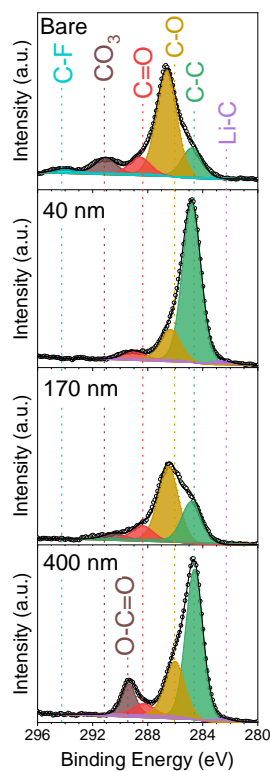


**Figure S12.** Core-level C 1s XPS spectra of Li metal anodes after 20 cycles in Li-S cells with bare, 40-nm, 170-nm, and 400-nm coated pDVB-co-DMAMS-coated separators.

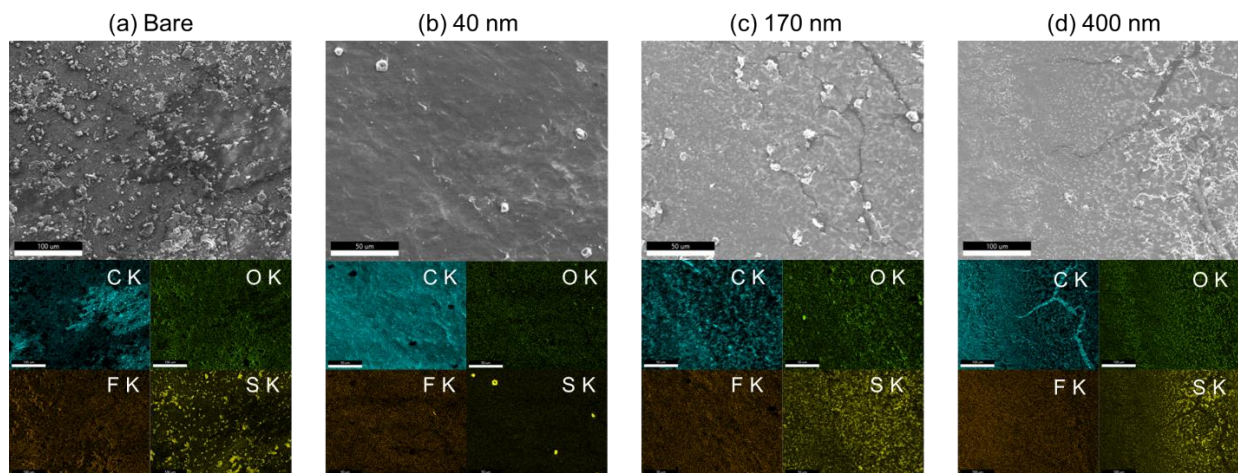


**Figure S13.** SEM-EDS mapping of the separator surface facing the cathode after 20 cycles for (a) bare, (b) 40nm-, (c) 170nm-, and (d) 400nm-iCVD@PE separators.

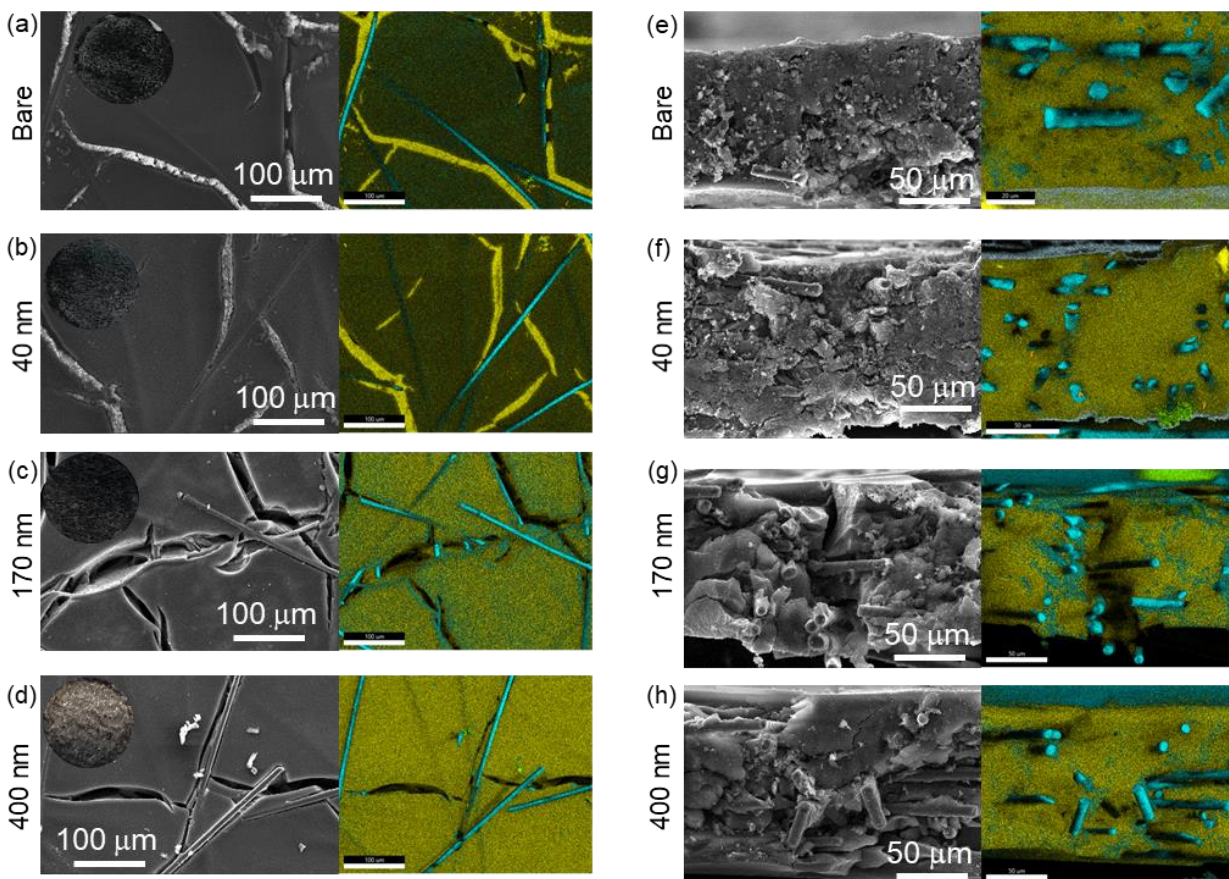


**Figure S14.** (a-d) SEM images and EDS maps of S@CNFP cathode surface from cells with bare, 40nm-, 170nm-, and 400nm-iCVD@PE separators. Inset: optical image of cathode. (e-h) Cross-sectional SEM image and EDS maps for each cathode. The colors in the EDS map correspond to the following elements: yellow – S, blue – C, and green – O.

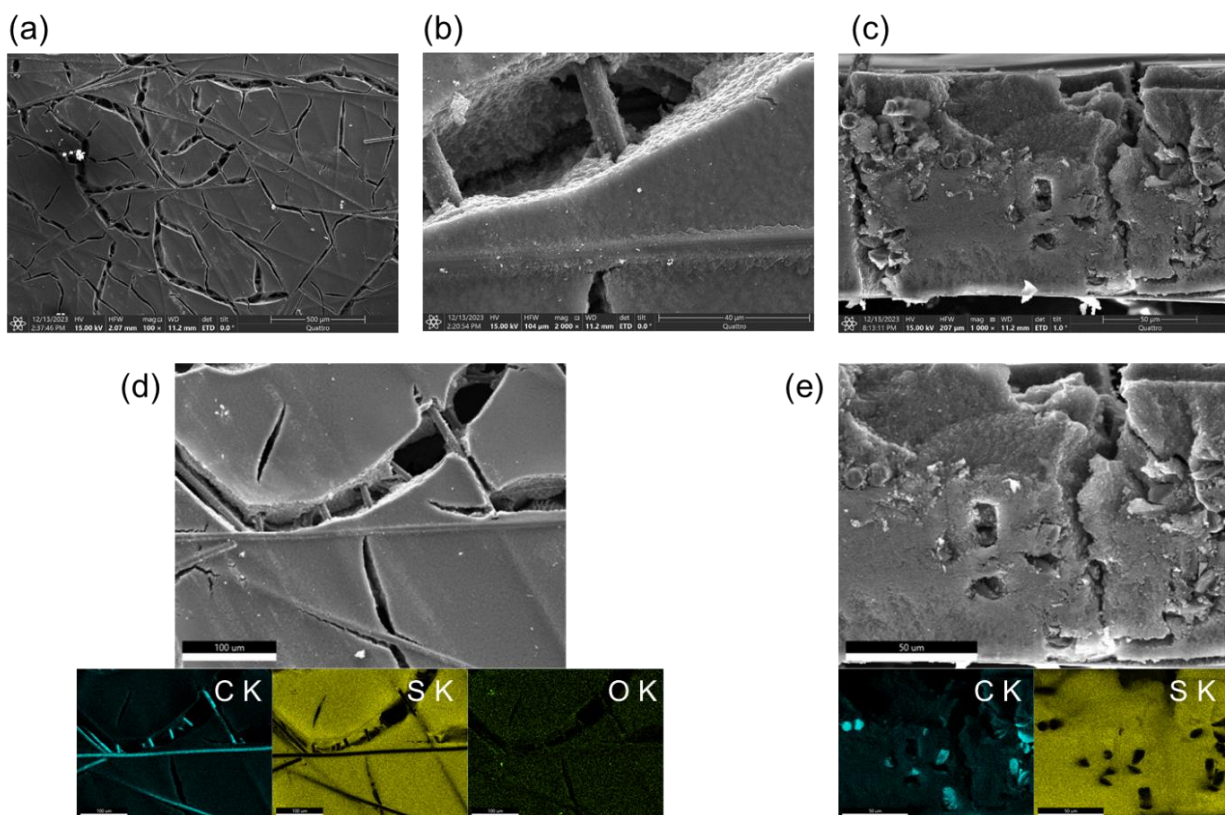


**Figure S15.** SEM imaging of pristine S@CNFP cathodes at the (a-b) surface and (c) cross-section. EDS mapping of (d) surface and (e) cross-section of the cathodes.

### Additional Information on Atomistic Simulations:

Computation of  $\text{Li}_2\text{S}_n$  binding energy to the DMAMS monomer used  $22.5 \text{ \AA}$  cubic simulation boxes. The energy is referenced to isolated DMAMS and  $\text{Li}_2\text{S}_n$  molecules. The lowest-energy points represent fully relaxed DMAMS– $\text{Li}_2\text{S}_n$  pairs, with binding energies of 0.93, 0.93, and 0.95 eV for  $\text{Li}_2\text{S}_4$ ,  $\text{Li}_2\text{S}_6$ , and  $\text{Li}_2\text{S}_8$  respectively. The vdW interaction contributes 0.18, 0.24, and 0.25 eV respectively. The primary interaction between DMAMS and  $\text{Li}_2\text{S}_n$  is a Lewis base interaction. The remaining points show configurations that are relaxed subject to a fixed N–Li distance. Curves show fits to a Morse potential:

$$V(r) = D_e(1 - e^{-a(r-r_e)})^2 - D_e.$$

Here  $D_e$  is set to the binding energy of a fully relaxed bonded pair,  $r_e$  is the relaxed N–Li distance, and  $a$  is a fitting parameter. The fitted values of  $a$  are 1.36, 1.25, and  $1.30 \text{ \AA}^{-1}$  for  $\text{Li}_2\text{S}_4$ ,  $\text{Li}_2\text{S}_6$ , and  $\text{Li}_2\text{S}_8$  respectively.

Computation of binding energy of  $\text{Li}_2\text{S}_n$  to the graphene monolayer used a rectangular  $17.3 \text{ \AA} \times 17.1 \text{ \AA}$  graphene supercell (a  $\begin{pmatrix} 7 & 0 \\ 4 & 8 \end{pmatrix}$  supercell of the primitive hexagonal cell) and a  $25 \text{ \AA}$  vacuum space between layers. Total binding energies were 0.42, 0.57, and 0.41 eV for  $\text{Li}_2\text{S}_4$ ,  $\text{Li}_2\text{S}_6$ , and  $\text{Li}_2\text{S}_8$  respectively. The vdW contributions (0.34, 0.45, and 0.40 eV respectively) dominate the binding energies.

Calculations of solvation effects used a MACE interatomic potential.<sup>1</sup> The potential was fine-tuned starting from the MACE-MP-0 foundation model<sup>2</sup> using a dataset of DFT energies, forces, and stresses of 2836 atomic configurations (with an average of about 200 atoms each, for a total of 2836 energies, 561,268 forces, and 17,016 stresses) split into 80% training, 10% validation, and 10% test. The DFT calculations were done in VASP using the PBE functional<sup>3</sup>, the DFT-D3 method of Grimme with zero-damping<sup>4</sup>, and a plane-wave energy cutoff of 500 eV. The Brillouin zone was sampled with a density of at least 64 points per  $\text{\AA}^{-3}$ : Gamma-point only for larger cells, and otherwise Monkhorst-Pack as generated by the “automatic\_density\_by\_vol” method in pymatgen.<sup>5</sup> The configurations were primarily DFT snapshots from VASP MD simulations in on-the-fly machine-learning training mode<sup>6</sup> (ML\_MODE = train), though some configurations from relaxation strings were also included. The fine-tuning procedure achieved low root-mean-square errors (RMSE) compared to the test set: 1.5 meV/atom in energies and 48.2 meV/ $\text{\AA}$  in forces.

The binding enthalpy including solvation is defined by:

$$H_{\text{bind}}^{\text{sol}} = -E_{\text{avg}}[\text{Li}_2\text{S}_6 + \text{DMAMS} + \text{sol}] - E_{\text{avg}}[\text{sol}] \\ + E_{\text{avg}}[\text{Li}_2\text{S}_6 + \text{sol}] + E_{\text{avg}}[\text{DMAMS} + \text{sol}]$$

Here “sol” stands for a set of solvent molecules (5 DME and 7 DOL) and  $E_{\text{avg}}$  indicates the average potential energy over a MD trajectory. All configurations were initialized in  $13.5 \text{ \AA}$  cubic simulation boxes with periodic boundary conditions. After an initial relaxation and 250 ps equilibration at 300 K and zero pressure (NPT), the energies of each configuration were averaged over a 1.35 ns NPT trajectory, sampled every 50 fs. The simulations were carried out in LAMMPS<sup>7</sup> with a 1 fs timestep and a Nose-Hoover thermostat/barostat. The error is the sum of squares of the standard error of the mean (SEM) of each sample:

$$\Delta H_{\text{bind}}^{\text{sol}} = \left( \text{SEM}[\text{Li}_2\text{S}_6 + \text{DMAMS} + \text{sol}]^2 + \text{SEM}[\text{sol}]^2 + \text{SEM}[\text{Li}_2\text{S}_6 + \text{sol}]^2 \right. \\ \left. + E_{\text{avg}}[\text{DMAMS} + \text{sol}]^2 \right)^{\frac{1}{2}}$$

To calculate the SEM, an effective sample size must be established, since the energies of snapshots separated by 50 fs are clearly correlated, so they cannot be treated as independent samples of the energy distribution. We remove the effect of correlations from our error estimate by block-averaging the trajectories in successively larger blocks, then calculating the error assuming each block is an independent sample. For correlated blocks, the estimated error increases with block size. Once the blocks are large enough that successive blocks are uncorrelated, the estimated error saturates.<sup>8</sup> The optimum block size is determined by the heuristic given in Lee et. al<sup>8</sup>. The estimated error may be used to establish an effective sample size, as shown in Table S1.

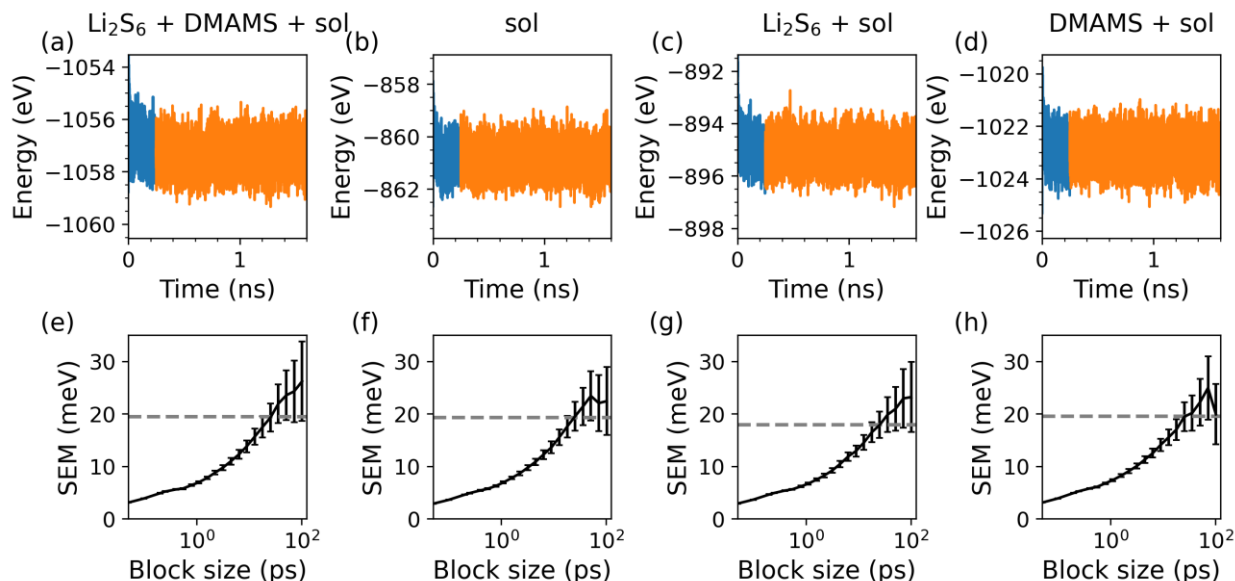


**Figure S16.** (a-d): Potential energy of MD trajectories using the fine-tuned MACE potential. The equilibration portion of the trajectory is shown in blue and the sampling portion is shown in orange. (e-h): Estimated error as a function of block size. The optimum block size determines the best error estimate, indicated by a gray line. Saturation behavior at larger block sizes indicates a converged error estimate.

**Table S1.** The average energy, standard deviation, effective number of samples, and SEM for each calculation.

Calculation	Energy (eV)	Std. Dev. (eV)	$n_{\text{samples}}$	SEM (eV)
Li <sub>2</sub> S <sub>6</sub> + DMAMS + sol	-1057.400	0.506	675	0.0195
sol	-860.904	0.468	589	0.0193
Li <sub>2</sub> S <sub>6</sub> + sol	-895.155	0.474	703	0.0179
DMAMS + sol	-1023.003	0.506	670	0.0195

## References:

1. I. Batatia, D. P. Kovacs, G. Simm, C. Ortner and G. Csányi, *Adv Neural Inf Process Syst*, 2022, **35**, 11423-11436.
2. I. Batatia, P. Benner, Y. Chiang, A. M. Elena, D. P. Kovács, J. Riebesell, X. R. Advincula, M. Asta, W. J. Baldwin and N. Bernstein, *arXiv preprint arXiv:2401.00096*, 2023.
3. J. P. Perdew, K. Burke and M. Ernzerhof, *Phys. Rev. Lett.*, 1996, **77**, 3865-3868.
4. S. Grimme, J. Antony, S. Ehrlich and H. Krieg, *J. Chem. Phys.*, 2010, **132**, 154104Advanced Electronic Materials.
5. A. Jain, G. Hautier, C. J. Moore, S. Ping Ong, C. C. Fischer, T. Mueller, K. A. Persson and G. Ceder, *Comput. Mater. Sci.*, 2011, **50**, 2295-2310.
6. R. Jinnouchi, J. Lahnsteiner, F. Karsai, G. Kresse and M. Bokdam, *Phys. Rev. Lett.*, 2019, **122**, 225701.
7. A. P. Thompson, H. M. Aktulga, R. Berger, D. S. Bolintineanu, W. M. Brown, P. S. Crozier, P. J. in 't Veld, A. Kohlmeyer, S. G. Moore, T. D. Nguyen, R. Shan, M. J. Stevens, J. Tranchida, C. Trott and S. J. Plimpton, *Comput. Phys. Commun.*, 2022, **271**, 108171.
8. R. M. Lee, G. J. Conduit, N. Nemeč, P. López Ríos and N. D. Drummond, *Phys. Rev. E*, 2011, **83**, 066706.